https://doi.org/10.5194/egusphere-2026-1235
Preprint. Discussion started: 19 March 2026

Mobility of dry granular debris flows over erodible beds: Experimental insights into the influence of flow–bed inertia

Katharina Wetterauer[1], Sebastian Müller[1], Michael Krautblatter[2], Shiva P. Pudasaini[2], and Ivo Baselt[1]

[1]Chair of Hydromechanics and Hydraulic Engineering, University of the Bundeswehr Munich, Neubiberg, Germany
[2]Chair of Landslide Research, Technical University of Munich, Munich, Germany

Correspondence: Katharina Wetterauer (katharina.wetterauer@unibw.de)

Abstract. Debris-flow mobility responds sensitively to erosion and entrainment that exchange mass and momentum across the flow-bed interface. Yet, the mechanical controls that cause some debris flows to accelerate during erosion while others decelerate are insufficiently understood. Recent theory attributes this divergent behavior to inertial contrasts between the moving mass and the erodible bed, suggesting that incorporating inertially weaker, neutral, or stronger substrate into the flow enhances, maintains, or reduces flow mobility, respectively. Here, we conducted flume experiments and surface-based measurements to assess how the inertia of the erodible bed affects the flow kinematics, erosion, entrainment, and runout of dry granular single-phase debris flows. We systematically imposed inertial contrasts by releasing a quartz slide of constant solid density over erodible beds with lower, equal, and higher solid densities representing inertially weak, neutral, and strong scenarios, and compare these alongside a reference case without erosion. Each scenario was repeated for fine sand and a sand–gravel mixture. Our results reveal consistent behavior across both particle-size distributions. Debris flows over low-density beds exhibit higher apparent mean erosion rates, faster flow fronts before deposition, and longer runout lengths, whereas flows over equal- and high-density beds evolve similarly, with shallower erosion, slower flow fronts, and shorter, more compact deposits. Relative to the neutral scenario, the entrainment of low-density material thus appears to enhance debris-flow mobility, while incorporating high-density material does not lead to the anticipated mobility loss. This asymmetric response suggests that solid-density contrasts alone are insufficient to explain the observed trends under the experimental conditions considered here. Differences in particle shape and internal friction likely also contribute. Whereas the low-density bed comprises more spherical particles with a lower friction angle facilitating entrainment, the equal- and high-density beds consist of angular particles with similar and higher internal friction angles, leading apparently to similar resistance to erosion despite their divergent densities. However, resolving whether more subtle differences persist between the inertial scenarios will require direct observations at the flow–bed interface to capture grain-scale dynamics and temporal variability in erosion intensity.

1 Introduction

Debris flows are highly dynamic natural hazards that shape mountain landscapes through erosion and deposition. Understanding their flow dynamics is essential for predicting future debris-flow activity in a changing climate and for reconstructing

https://doi.org/10.5194/egusphere-2026-1235
Preprint. Discussion started: 19 March 2026

long-term landscape evolution (e.g., Rickenmann, 1999; Reid et al., 2011; Roelofs et al., 2023). Yet, the physical mechanisms behind the high mobility observed in some erosive debris flows remain debated. Erosion of sediment from the bed and entrainment into the flow are thought to play a key role because they modify the total flow volume and can influence mobility through mass and momentum transfer (e.g., Hungr et al., 2005; Mangeney et al., 2007; Santi et al., 2008; Iverson et al., 2011). However, responses are not uniform: some debris flows disproportionally increase their volume and become highly mobile and destructive through entrainment, whereas others decelerate despite eroding (e.g., Hungr et al., 2005; Mangeney et al., 2007; Pudasaini and Krautblatter, 2021). Processes of erosion and entrainment are increasingly incorporated into debris-flow mobility models, accounting for mass production (e.g., McDougall and Hungr, 2005; Medina et al., 2008; Iverson, 2012; Frank et al., 2015) and mechanically including momentum production (Pudasaini and Fischer, 2020). However, the lack of a unified erosion theory and the mechanical complexity of flow–bed interactions still lead to large discrepancies among model equations and outcomes (De Haas et al., 2020). Additionally, many debris-flow models rely on poorly constrained equations or parameters, highlighting the need for data obtained under controlled and reproducible conditions (Iverson et al., 2011).

Controlled flume experiments have helped to constrain key parameters that correlate with the erosion potential of debris flows, primarily by systematically varying either the initial flow conditions or the bed characteristics while keeping the other constant. For example, when flow conditions are varied, granular single-phase flow experiments show that a greater flow mass intensifies bed erosion and entrainment (Lu et al., 2016) and enlarges the eroded zone, resulting in higher mobility and longer runout (Liu et al., 2023). Two-phase debris-flow experiments further reveal that water- or gravel-rich flows are more erosive than clay-rich flows (De Haas and Van Woerkom, 2016; Roelofs et al., 2022), with erosion largely controlled by basal shear stress (De Haas and Van Woerkom, 2016). Erosion increases linearly with higher water and gravel contents, as pore-pressure transfer to the bed and impact forces are enhanced, respectively. Increasing clay content, however, alters interstitial fluid viscosity and pore-pressure dynamics, leading to a non-linear erosion response (Roelofs et al., 2022). Runout analyses additionally indicate that higher water content increases entrainment volume, producing flatter, wider, and longer deposits (Pandey and Satyam, 2025). Instead, varying the bed characteristics demonstrates also the role of the mechanical and hydraulic properties of the erodible substrate. Erosion rates decrease as bed sediment becomes coarser (Egashira et al., 2001; Papa et al., 2004). Small-scale (Roelofs et al., 2023) and large-scale experiments (Reid et al., 2011; Iverson et al., 2011) show that increasing bed water content facilitates bed entrainment through elevated pore pressures and reduced effective basal friction, promoting higher flow velocities, mass and momentum growth, and longer runout. Measurements from natural events support these findings, indicating that high pore-water pressures within the bed coincide with sediment-entrainment phases (Berger et al., 2011) and that debris flows over saturated beds grow faster and attain more volume than those over drier beds (McCoy et al., 2012). Besides, variations in bed clay content appear to influence the contraction–dilation behavior of the bed, with an optimum clay content at which undrained loading conditions and liquefaction of the upper bed layer produce maximum erosion (Roelofs et al., 2023). Overall, these experimental insights highlight the mechanical complexity of processes across the flow–bed interface, which current theoretical models only partially capture.

https://doi.org/10.5194/egusphere-2026-1235
Preprint. Discussion started: 19 March 2026

A recent theoretical mobility model, proposed by Pudasaini and Krautblatter (2021), offers a mechanical explanation that links the erosion and mobility of landslides through bed inertia. For effectively single-phase flows, their approach derives mobility from the fundamental balance equations of mass, momentum, and energy rather than from empirical correlations. In this framework, erosion not only increases the landslide volume but also alters the energy budget of the moving mass by changing its inertia depending on the mechanical properties of the entrained bed sediment. According to the Pudasaini and Krautblatter (2021) model, three distinct energy regimes arise from the inertial contrast between the moving slide and the erodible bed. Mobility remains unchanged when erosion proceeds under inertially neutral conditions, where the slide and bed material exhibit equal inertia and no net gain or loss of flow momentum and energy occurs. In contrast, mobility increases through the erosion of an inertially weaker bed, which introduces mechanically weaker material into the moving slide, enhancing flow momentum and energy. Conversely, mobility decreases through the erosion of an inertially stronger bed, as mechanically stronger material is entrained into the slide, causing momentum and energy dissipation despite continued erosion and volume gain. Accordingly, these contrasting energy regimes would directly govern landslide runout, as mobility gain or loss results in longer or shorter travel distances. Although this formulation provides a clear mechanical basis for how and when erosion enhances or reduces landslide mobility, the predicted processes have not yet been empirically confirmed and parameterized.

The present study examines how variations in bed inertia influence the mobility and runout of erosive debris flows in a series of small-scale flume experiments. We conducted dry granular single-phase debris-flow experiments in a steep channel, systematically varying the inertial contrast between sliding and bed material. We tested three erosive scenarios that represent inertially weak, neutral, and strong conditions, as well as a reference scenario without erosion. Each scenario was performed for a finer (sand-sized) and a coarser (sand-to-gravel-sized) fraction to assess potential grain-size-dependent effects. We combine high-resolution measurements of flow surface and deposit surface with qualitative analyses of the deposit's internal structure. This integrated analysis directly relates debris-flow dynamics, erosion intensity, and depositional form, to assess from different stages of the event how erosion at mechanically contrasting flow–bed interfaces affects flow mobility. Our empirical findings therefore provide a first-order, surface-based evaluation of how the inertia-based mobility concept proposed by Pudasaini and Krautblatter (2021) aligns with experimentally observed debris-flow behavior.

2 Material and Methods

2.1 Targeted inertial scenarios and materials

Inertia describes the resistance of moving material to a change of its velocity in magnitude and direction. In continuum mechanics, inertia is, beside velocity, proportional to mass density for a given material volume. Consequently, debris-flow inertia can be modified by incorporating mass from an erodible bed with a different density, solid volume fraction, friction, or different velocity. To test the inertia-based mobility concept proposed by Pudasaini and Krautblatter (2021), we designed a setup for dry granular debris-flow experiments, where the dry debris flow overrides a dry erodible bed initially at rest. In the present study,

https://doi.org/10.5194/egusphere-2026-1235
Preprint. Discussion started: 19 March 2026

any change in inertia can therefore only arise from a change in density. Based on this density–inertia relationship, we use sliding materials and erodible beds that exhibit distinct contrasts in solid density. Accordingly, materials with higher density are considered inertially (mechanically) stronger, whereas low-density materials are considered inertially (mechanically) weaker. As this study provides an initial experimental assessment of the hypotheses by Pudasaini and Krautblatter (2021) and focuses on testing the predicted mechanical behavior under controlled dry granular conditions, we do not aim to achieve full dynamic similarity with natural debris flows. Instead, all analyses are conducted at a consistent laboratory scale, and our interpretations are based on relative differences between weak, neutral, and strong scenarios rather than on absolute scaling to natural debris flows.

Four slide–bed configurations called "scenarios" were tested by keeping the initial sliding material constant while systematically varying the bed material: (i) an inertially weak scenario, where a quartz slide overrode a low-density bed made of expanded glass ($\rho_{\mathrm{Glass}} \approx 400$–$600\ \mathrm{kg\,m^{-3}}$; Fig. 1a), (ii) an inertially neutral scenario, where both slide and bed consisted of quartz with equal density ($\rho_{\mathrm{Qtz}} = 2700\ \mathrm{kg\,m^{-3}}$; Fig. 1b), (iii) an inertially strong scenario, where a quartz slide overrode a high-density bed made of magnetite ($\rho_{\mathrm{Mag}} = 4800\ \mathrm{kg\,m^{-3}}$; Fig. 1c), and (iv) a reference scenario without erosion, where the quartz slide moved over a rigid, rough-coated plywood surface (Fig. 1d). In the three erosive scenarios (i–iii), the quartz thus served as the inertial reference relative to the erodible bed material. Its initially released volume was identical in all experiments and consisted of 130 kg dry quartz sand (Fig. 1b). In addition, to examine whether potential inertial effects vary across particle-size fractions, the four scenarios were each conducted in two experimental series using a fine fraction (0.25–2 mm; "/f") composed of 100% sand, and a coarse fraction (0.25–8 mm; "/c") composed of 50% sand and 50% gravel (Fig. 1e).

The selection of materials was based on two main considerations: the use of natural sands to approximate the particle characteristics of natural debris-flow sediments, and the ability to efficiently separate slide–bed mixtures after the experiments to enable complete material reuse. Quartz and magnetite were chosen as natural sediments with angular particles and contrasting densities, and as they allowed efficient post-experimental magnetic separation of their mixture (Table 1, Fig. 1b, c). Expanded glass (PORAVER®), in contrast, is an artificial material composed of nearly spherical particles (Table 1, Fig. 1a). It was selected because no natural sediment with a distinctly lower density relative to quartz was available that could be efficiently separated for reuse. The buoyancy of the light expanded glass enabled complete separation of quartz–glass mixtures by their density contrast in a water bath. To ensure comparable particle-size distributions, quartz, expanded glass, and magnetite were each sieved into the previously defined fine and coarse fractions (Fig. 1e). Detailed material properties are listed in Table 1.

From here on, we refer to the materials as "Glass", "Qtz", and "Mag", and to the four scenarios as "Glass/f", "Qtz/f", "Mag/f", and "reference" for the fine-particle experiments or "Glass/c", "Qtz/c", "Mag/c", and "reference" for the coarse-particle experiments. Moreover, we use the term "slide" to refer specifically to the initially released Qtz–slide before its interaction with the erodible bed or to distinguish the overrunning from the erodible material. In all other cases we use "debris flow". We further emphasize that, for simplicity and as an initial step, all experiments were conducted in a dry state, representing single-phase flows. Accordingly, when the term "debris flow" refers to our tests, it specifically denotes these dry granular single-phase flows.

https://doi.org/10.5194/egusphere-2026-1235
Preprint. Discussion started: 19 March 2026

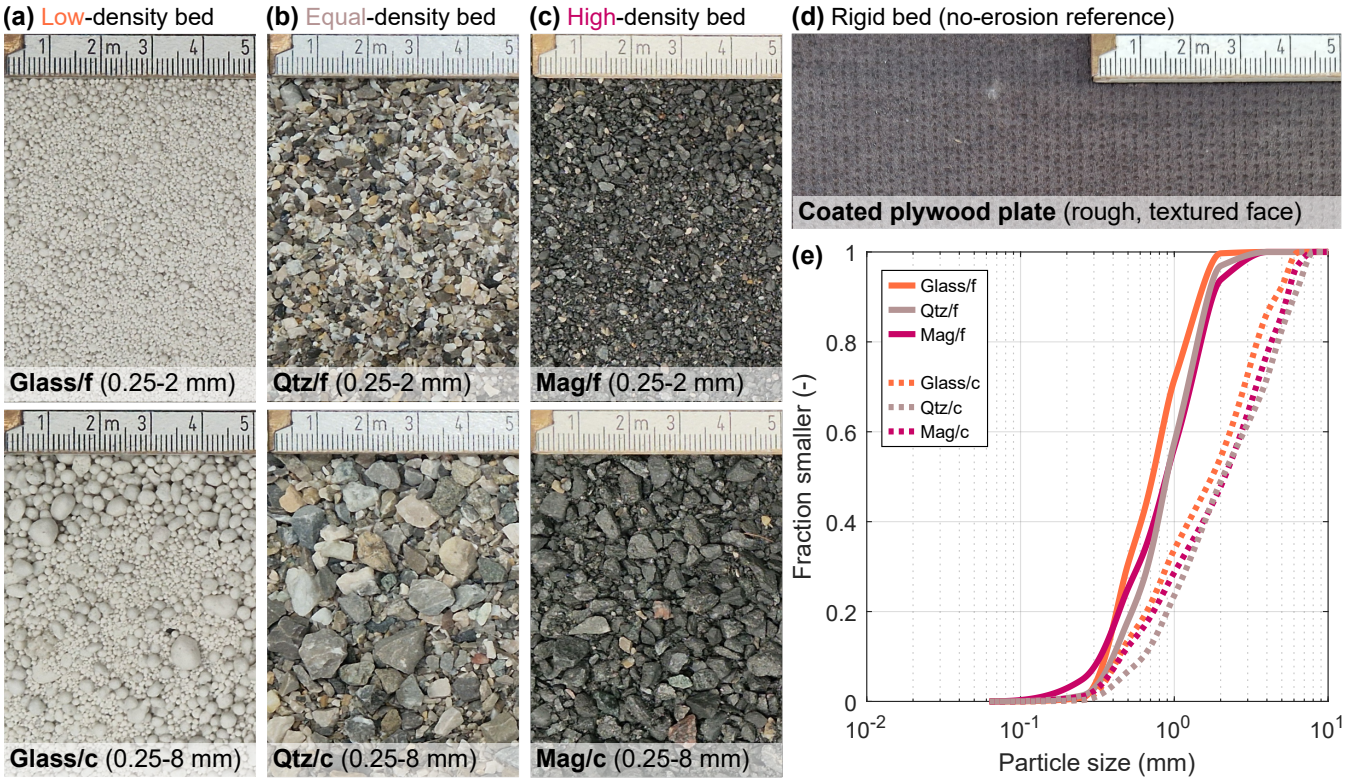

Figure 1. Materials used to simulate different inertial bed conditions in the conducted debris-flow experiments. (a-c) Erodible bed materials with (a) expanded glass for the inertially weak scenario, (b) quartz for the inertially neutral scenario, and (c) magnetite for the inertially strong scenario. (d) Coated plywood plate used as rigid bed for a reference case without erosion. (e) Cumulative particle-size distributions for fine (/f) and coarse (/c) fraction. Note that the quartz sand shown in (b) was used as initial sliding material in all experiments.

Table 1. Characteristics of the erodible materials used to simulate different inertial bed scenarios.

Erodible bed material	Relative inertia of bed to slide	Particle size		Solid particle density ($kg\,m^{-3}$)	Dry bulk density ($kg\,m^{-3}$)	Internal friction angle (°)	Basal friction angle* (°)
			(mm)				
Expanded Glass	inertially weak	Glass/f	0.25–2	580	300	29**	25**
		Glass/c	0.25–8	440	260	31**	23**
Quartz	inertially neutral	Qtz/f	0.25–2	2710	1360	37	31
		Qtz/c	0.25–8	2740	1530	39	30
Magnetite	inertially strong	Mag/f	0.25–2	4760	2620	35	29
		Mag/c	0.25–8	4830	2750	38	29

* Angle with respect to the coated plywood plates used as rigid bed surface in the flume setup.
** Due to the low friction angles, Glass was mixed with 4–5% water to stabilize and prevent self-induced failure on the 37° inclined flume.

https://doi.org/10.5194/egusphere-2026-1235
Preprint. Discussion started: 19 March 2026

2.2 Experimental flume

Debris-flow experiments were conducted at the Hydraulic Laboratory of the University of the Bundeswehr Munich, Germany, in a newly designed experimental debris-flow flume (Fig. 2). This flume consisted of a 5 m long and 0.26 m wide straight channel with 0.5 m high vertical sidewalls, forming a rectangular cross-section. Upstream of the channel, a funnel-shaped reservoir stored the 130 kg initial sliding material. It was filled by releasing Qtz vertically from a bag into the reservoir without pre-mixing to preserve natural variability and internal sorting, as these conditions better represent natural debris-flow initiation where material is rarely homogeneous. A flap operated by a pneumatic cylinder opened in a split second, releasing the Qtz into the channel. The 5 m long channel was divided into four distinct sections: (i) an upper rigid bed (2 m) made of rough-coated plywood, to allow the slide to develop and accelerate; (ii) a transitional bed (~1 m) containing a rigid lattice, shaped like a Lego brick, which was overfilled with erodible bed material to gradually adapt the slide to the erodible bed and prevent immediate scouring; (iii) an erodible bed (~1 m) with a thickness of 0.1 m; and (iv) a lower rigid bed (1 m) made of rough-coated plywood, to avoid extensive head erosion and sudden failure of the erodible bed section. Downstream of the channel, the slide–bed mixture entered a 3.4 m long and 2 m wide runout area, inclined by 10° to facilitate material outflow and reduce in-channel deposition resulting from the abrupt slope break and associated reduction of flow momentum. Except for the channel beds, all flume elements in contact with the flow were made of smooth materials with similarly low roughness (equivalent sand roughness $k_s \leq 0.01$ mm) to minimize frictional resistance. Acrylic glass was used for the reservoir and transparent front sidewall, PVC for the back sidewall, and smooth plywood for the runout area.

A steep flume inclination of 37° was used for all experiments to ensure sufficiently high sliding velocities and, therefore, a high erosive potential (e.g., De Haas and Van Woerkom, 2016; Lanzoni et al., 2017). This slope was close to the internal friction angle of the erodible Qtz and Mag beds (Table 1), representing the steepest angle at which these beds remained stable without spontaneous failure. However, due to the comparatively low internal friction angle of Glass, the Glass beds had to be stabilized with 4–5% water and were uniformly compacted to increase particle cohesion (Table 1). After each experiment, the flume was returned to a horizontal position for post-experimental measurements.

2.3 Instrumentation, measurements, and data processing

Flow height and flow-front velocity were derived from seven ultrasonic sensors (WayCon UFP-400; 30–400 mm range, 60 ms sampling interval, ± 1 mm accuracy) installed normal to the bed along the channel centerline (us1–us7; Fig. 2). The sensors were positioned in systematic intervals to capture both the temporal evolution of the flow at specific locations and its spatial development downslope. To prevent potential data gaps from signal loss, most sensors were installed in pairs: us1–us2 at the end of the upper rigid bed, us3 above the transitional bed, us4–us5 above the erodible bed, and us6–us7 at the end of the lower rigid bed. Data recording was synchronized with the reservoir opening, as the sensor trigger was coupled to the flap-release mechanism. Postprocessing of the records was performed in MATLAB®. For each sensor, flow height was derived by subtracting the mean value of the first-second measurements (representing the initial bed level at flow height 0 cm) from every

https://doi.org/10.5194/egusphere-2026-1235
Preprint. Discussion started: 19 March 2026

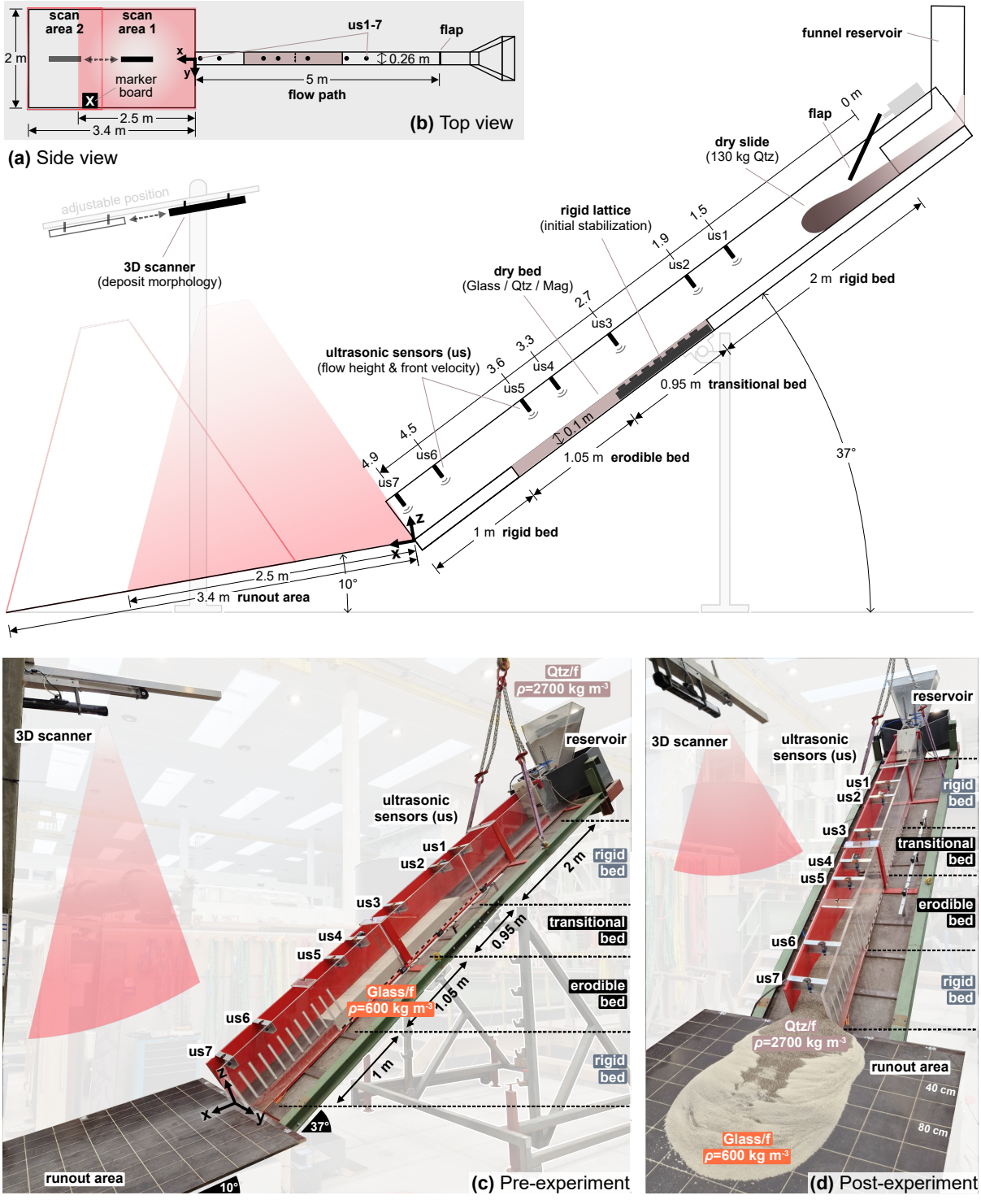

Figure 2. Experimental flume setup. (a) Side- and (b) top-view schematic. (c) Flume with planar erodible bed and filled reservoir before the experiment. (d) Deposit after the experiment. Flume sections and measurement positions are indicated. Photographs are from Exp5 (Glass/f).

https://doi.org/10.5194/egusphere-2026-1235
Preprint. Discussion started: 19 March 2026

subsequent data point in the time series. The signals were then smoothed using a moving-average filter over 0.1 s intervals. At the rigid bed sections, the resulting flow height corresponds directly to the actual slide thickness, as the bed surface remained fixed at 0 cm. At the erodible bed, however, ongoing erosion lowered the surface, so records us4–us5 represent an apparent flow height that reflects a mixed signal of both temporal variations in slide thickness and bed-level change. Flow-height values can thus even become negative when erosion becomes deeper than slide thickness. Flow-front arrival was defined as the moment when the flow height first exceeded a 1 mm threshold. Flow-tail passage was defined as the first time after flow-front arrival that the decreasing flow height crossed the mean height calculated over the last 1.5 s of the ultrasonic record, after the flow had completely passed the sensor. Flow-front velocity was calculated from the ratio of the traveled distance from the reservoir flap to each sensor (Fig. 2a) and the respective time of flow-front arrival.

We also derived an apparent mean erosion rate at sensor us4, calculated as the ratio between the final erosion depth and the duration of debris-flow passage at us4. We refer to this rate as "apparent" because it does not capture the temporal variability of the erosion process but represents an average over the entire flow duration at this single location. In reality, however, the flow tail likely exerts insufficient shear stress to sustain erosion and instead promotes material deposition onto the erodible bed (e.g., De Haas et al., 2015), leading to an underestimation of the final erosion depth that reflects the bed surface after tail passage.

Deposit morphology was mapped using a 3D-surface scanner (MotionCam-3D L Blue LC3R; 2.5 × 2.1 m scan area, 2 Mpx resolution, <1.25 mm accuracy) mounted above the runout area with perpendicular view to the 10°-inclined surface (Fig. 2). The scanner was positioned along the centerline, and x, y, z coordinates were referenced with a marker board fixed to one lateral rim of the scan area. For deposits extending beyond the scan area, the scanner was repositioned downstream by a guide rail system to capture the whole runout area. A second scan overlapping the first at the marker board position was acquired and merged with the first by exact alignment at the marker board, establishing a shared coordinate system (Fig. 2a,b). Scans were performed with the flume in a horizontal position to prevent signal reflection from the channel outlet, which protruded into the scan cone when the flume was inclined (Fig. 2a). Therefore, the morphologies presented below represent only material deposited on the runout area but do not account for in-channel deposition. Postprocessing of the 3D point clouds was carried out in MATLAB®. Deposits were first isolated by subtracting a reference scan of the planar, empty runout area. In a subsequent cluster analysis based on a minimum Euclidean distance of 5 mm, only the coherent deposit bodies were retained and disconnected particles were excluded. Finally, the remaining point clouds were converted into 3D-volume models using triangulation-based natural neighbor interpolation with a grid resolution of 3 mm. From the 3D-volume models, geometric and volumetric parameters of the mixed slide–bed deposits on the runout area were determined, including the deposit's length (L), width (W), maximum height, extent ratio (L/W), covered area, volume, center of volume, as well as the travel angle, which is defined here as the inclination between the deposit's center of volume and the lower edge of the reservoir outlet (Fig. 2a). Note that the center of volume should not be interpreted as the center of mass, since the mixed slide–bed deposits can contain materials of varying densities.

The internal structure of the Qtz–Glass and Qtz–Mag deposits on the runout area was examined qualitatively by slicing the deposits laterally into regular cross sections. Each profile was created by inserting a 2 mm thin glass plate vertically into

https://doi.org/10.5194/egusphere-2026-1235
Preprint. Discussion started: 19 March 2026

the deposit and capturing the exposed section with a camera, after the material in front of the glass plate had been removed. This qualitative approach was not applied to Qtz–Qtz deposits, as the Qtz bed was not colored to preserve its natural surface properties and ensure identical conditions and material reusability, making particles from slide and bed indistinguishable.

2.4 Experimental reproducibility

To evaluate reproducibility, a total of 24 debris-flow experiments (Exp1–Exp24) were performed, 12 for each material size fraction. Both fine and coarse experiments comprised all four scenarios (weak, neutral, strong, and reference), with every scenario repeated three times. To maintain consistent conditions, all experiments followed the same sequence of preparation and operation steps. The full set of debris-flow experiments is summarized in Table 2 and frontal photographs of all experiments are provided in the Supplement in Figures S1 and S2.

Table 2. Experimental debris-flow conditions as well as deposit characteristics.

Experiment					**Deposit measures**						
Exp ID	**Fraction**	**Slide**	**Bed (scenario)**	**Rep**	**Length** (cm)	**Width** (cm)	**Height** (cm)	**Area** (m^2)	**Volume** (L)	**L/W**** (−)	**Travel angle***** (°)
Exp1*	fine	Qtz	Qtz (neutral)	1	97	92	22	0.7	53	1.0	34.2
Exp2	fine	Qtz	Qtz (neutral)	2	85	94	22	0.7	56	0.9	34.2
Exp3	fine	Qtz	Qtz (neutral)	3	85	88	21	0.6	49	1.0	34.3
Exp4	fine	Qtz	Glass (weak)	1	157	94	16	1.3	74	1.7	32.7
Exp5*	fine	Qtz	Glass (weak)	2	157	92	15	1.3	75	1.7	32.5
Exp6	fine	Qtz	Glass (weak)	3	159	90	15	1.2	68	1.8	32.5
Exp7*	fine	Qtz	Mag (strong)	1	90	89	21	0.7	51	1.0	34.3
Exp8	fine	Qtz	Mag (strong)	2	96	84	19	0.7	48	1.1	34.3
Exp9	fine	Qtz	Mag (strong)	3	96	85	19	0.7	46	1.1	34.3
Exp10	fine	Qtz	reference	1	135	82	16	1.0	60	1.6	33.5
Exp11	fine	Qtz	reference	2	140	83	16	1.0	67	1.7	33.3
Exp12*	fine	Qtz	reference	3	146	83	15	1.1	71	1.7	33.1
Exp13	coarse	Qtz	Qtz (neutral)	1	127	78	17	0.9	46	1.6	33.9
Exp14*	coarse	Qtz	Qtz (neutral)	2	127	82	18	0.9	49	1.5	33.9
Exp15	coarse	Qtz	Qtz (neutral)	3	132	82	18	0.9	51	1.6	33.9
Exp16	coarse	Qtz	Glass (weak)	1	316	129	11	3.1	91	2.4	29.2
Exp17	coarse	Qtz	Glass (weak)	2	336	135	10	3.6	91	2.5	29.1
Exp18*	coarse	Qtz	Glass (weak)	3	303	125	11	2.9	89	2.4	30.0
Exp19	coarse	Qtz	Mag (strong)	1	128	83	17	0.9	51	1.5	33.7
Exp20*	coarse	Qtz	Mag (strong)	2	129	79	17	0.9	50	1.6	33.8
Exp21	coarse	Qtz	Mag (strong)	3	121	79	17	0.8	47	1.5	33.9
Exp22*	coarse	Qtz	reference	1	245	114	12	1.9	83	2.2	27.8
Exp23	coarse	Qtz	reference	2	242	104	11	1.7	81	2.3	27.9
Exp24	coarse	Qtz	reference	3	228	100	13	1.6	81	2.3	28.6

* Runs selected for detailed analysis and illustration in this study (see Sect. 2.4).
** Length-to-width ratio.
*** Defined as the inclination between the deposit's center of volume and the lower edge of the reservoir outlet.

https://doi.org/10.5194/egusphere-2026-1235
Preprint. Discussion started: 19 March 2026

From the three repetitions per scenario, one representative run was selected for detailed analysis and illustration: fine fraction – Glass/f (Exp5), Qtz/f (Exp1), Mag/f (Exp7), reference (Exp12); coarse fraction – Glass/c (Exp18), Qtz/c (Exp14), Mag/c (Exp20), reference (Exp22). The selection was based on the best overall agreement in flow-front arrival time and early-stage flow-height evolution across the four scenarios recorded at sensor us2 (see Sect. 3.1.1). This sensor served as a control for consistent initial debris-flow behavior for the four scenarios, as the flow at this location consisted solely of the released Qtz–slide, which was identical in all runs within a size fraction. Unless stated otherwise, the data presented hereafter refer to these representative runs.

3 Results

3.1 Spatiotemporal debris-flow evolution and bed erosion

The flow-height hydrographs from the ultrasonic sensors illustrate the spatiotemporal evolution of fine and coarse debris-flow passage along the flume channel (Fig. 3). We present below the data from us2, us4, and us6, which capture the key stages of debris-flow progression: pre, during, and post erosion. The remaining sensors recorded equivalent trends and are shown in the Supplement to avoid redundancy (Supplement Figs. S3 and S4). Flow-height signals were highly reproducible across all repeated fine and coarse experiments.

3.1.1 Flow heights upstream the erodible bed

Before reaching the erodible bed (us2 in Fig. 3), flow heights show a nearly identical temporal evolution across all scenarios. The early Qtz–slides are characterized by a rapid rise and a more gradual subsequent decay in flow height. The timing of flow-front arrival and flow-tail passage is well defined and consistent. In the fine experiments, flow fronts reach us2 about 1.3 s after slide release and the slides pass within 5 s. They thicken up to 5 cm, with peak height occurring near the flow head. In the coarse experiments, flow fronts arrive at the same time but the slides pass within 4 s. Peak heights remain thinner at 3.5 cm and the association between peak height and flow front is less distinct.

3.1.2 Flow heights on the erodible bed and local bed erosion

At the erodible bed, (us4 in Fig. 3), flow fronts still arrive almost simultaneously across all scenarios. Yet, the temporal evolution of flow heights begins to diverge, the relative tendencies remaining the same in the fine and coarse experiments.

In the reference experiments without erosion, flow evolution resembles that observed at us2 but with a flatter passage. The fine debris flow passes within 5.0 s at maximum 4 cm thickness, while the coarse debris flow passes within 4.5 s reaching a peak height of 3 cm.

https://doi.org/10.5194/egusphere-2026-1235
Preprint. Discussion started: 19 March 2026

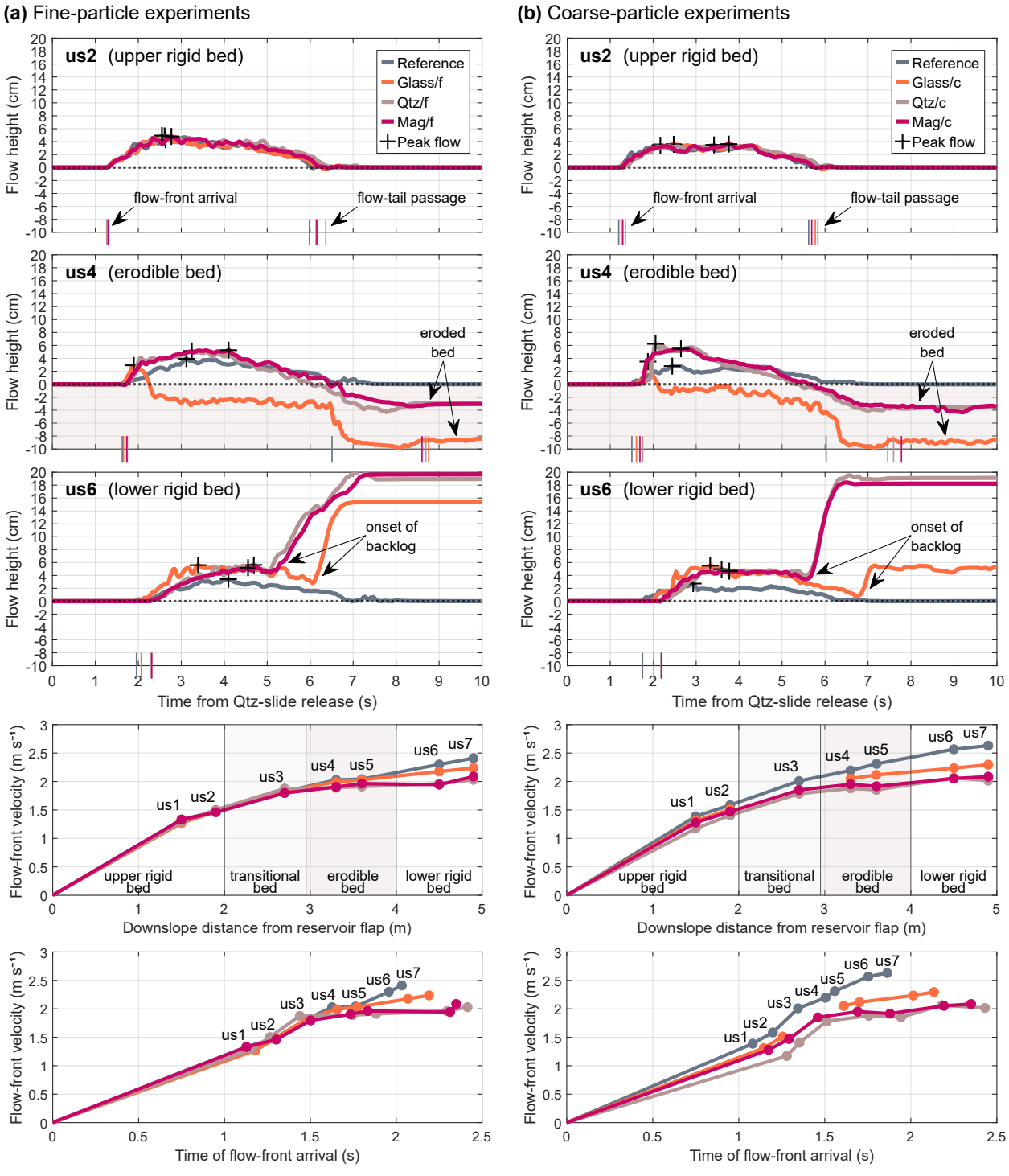

Figure 3. Spatiotemporal debris-flow evolution of (a) fine- and (b) coarse-particle experiments. From top to bottom: evolution of flow height over time at us2 (before the erodible bed), us4 (on/eroding the bed), and us6 (before the runout area), as well as flow-front velocity downslope, and over time. Representative runs are shown (see Sect. 2.4). Note that in (b), no data point is shown at us3 for the Glass/c experiment in the two lower panels due to a brief ultrasonic signal loss during flow-front passage. /f: fine particles; /c: coarse particles; us: ultrasonic sensor.

https://doi.org/10.5194/egusphere-2026-1235
Preprint. Discussion started: 19 March 2026

In the erosive experiments, by contrast, flow fronts steepen immediately upon arrival, and the duration of debris-flow passage increases compared to us2. Fine debris flows pass the sensor in about 7 s, whereas coarse debris flows pass within 6 s, developing slightly steeper fronts. Yet, the magnitude and manner of bed erosion and surface lowering differ. In the Glass experiments, flow-height evolution follows a distinct three-step pattern: a steep, instantaneous front coincides with peak-flow height, followed by an abrupt first decline around 2 s after slide release, during which the debris-flow surface drops below the original bed level, and a second, more pronounced decline toward the end of the event around 6.5 s after slide release. After debris-flow passage, nearly the entire 10 cm thick bed is eroded. In the fine experiment (Glass/f), the successive drops reach -2.5 and -8.7 cm below the original bed surface, resulting in an apparent mean erosion rate of about 1.0 $\mathrm{cm\,s^{-1}}$. In the coarse experiment (Glass/c), the two successive drops reach about -1.0 and -8.9 cm, yielding an apparent mean erosion rate of about 1.2 $\mathrm{cm\,s^{-1}}$. In the Qtz and Mag experiments, flow heights evolve more gradually and behave almost congruently for both materials. The debris flows thicken initially toward peak flow and then decrease continuously, falling slightly below the original bed level. In the fine experiments (Qtz/f and Mag/f), flow heights reach an early peak, before declining to final erosion depths of approximately -2.9 and -3.1 cm, corresponding to apparent mean erosion rates of 0.3 and 0.4 $\mathrm{cm\,s^{-1}}$, respectively. In the coarse experiments (Qtz/c and Mag/c), peak height occurs earlier and the subsequent decline begins sooner. Final erosion depths of about -3.6 and -3.7 cm correspond to apparent mean erosion rates of 0.5 $\mathrm{cm\,s^{-1}}$.

3.1.3 Flow heights downstream the erodible bed

After erosion and before depositing on the runout area (us6 in Fig. 3), the timing of flow-front arrival appears to differ among the four scenarios, by a few tenths of a second. The references arrive first, followed by Glass, while Qtz and Mag reach the sensor last and simultaneously. Fine debris flows arrive a few milliseconds later than coarse debris flows. It is noted that flow heights in the erosive experiments show a distinct late rise, whereas the reference experiments display none. This late rise results from the debris flow backing up into the channel instead of being fully released onto the runout area, leading to in-channel deposition. The resulting backlog obscures the timing of the flow tail and is more pronounced for fine debris flows, which develop an earlier and stronger material accumulation than coarse debris flows.

3.1.4 Flow-front velocities downslope

Flow-front velocities overall increase with distance downslope, showing a steep initial rise that gradually tapers off in both fine and coarse experiments (Fig. 3). Velocities increase consistently along the upper rigid bed, reaching about 1.5 $\mathrm{m\,s^{-1}}$ at us2. On the erodible bed at us4, velocity trends begin to diverge among the four scenarios. In the reference experiments, velocities continue to increase approximately linearly downslope, reaching the highest final values of about 2.4 $\mathrm{m\,s^{-1}}$ in the fine and 2.6 $\mathrm{m\,s^{-1}}$ in the coarse debris flow. In the Glass experiments, flow-front velocities also increase along the erodible bed but with a slightly reduced gradient. Both fine and coarse debris flows reach about 2.2 $\mathrm{m\,s^{-1}}$ at us7, shortly before deposition. In

https://doi.org/10.5194/egusphere-2026-1235
Preprint. Discussion started: 19 March 2026

the Qtz and Mag experiments, velocities remain nearly constant once the debris flows encounter the erodible bed, with fine and coarse debris flows maintaining values around 2.0 $\mathrm{m\,s^{-1}}$ before the runout.

The time-dependent evolution of flow-front velocities, indicating flow-front acceleration, is likewise distinct (Fig. 3). In the reference experiments, the flow fronts accelerate nearly constantly over time, with the coarse debris flow showing a distinctly steeper increase than the fine debris flow. In the erosive experiments, acceleration is initially similar to the reference experiments but begins to decrease once the Qtz–slides encounter the erodible bed. This decline is less pronounced for Glass but clearly visible for Qtz and Mag, where the debris flows no longer accelerate after passing the erodible bed.

3.2 Runout characteristics

3.2.1 Deposit morphology

Deposit geometries differ clearly among the four scenarios and consistently in both size fractions (Figs. 4 and 5). All deposits are largely symmetric along the central downslope axis. Yet, most deposits show an artificial drop in height toward the channel outlet at $(0|0)$, due to partial material loss when the flume was leveled for surface scanning (see Sect. 2.3 and Supplement Fig. S5). This artifact, however, does not affect the overall depositional pattern. Below, the four scenarios for both size fractions are summarized. All repeated runs yielded highly consistent deposit morphologies, resulting in near-congruent shapes across the three repetitions (Table 2, Fig. 5; see Supplement Figs. S6 and S7 for all deposit contour plots). Runout lengths vary by less than $\pm 4\%$ from the mean of the three repeated runs for most scenarios and by a maximum of ~8% (Supplement Table S1).

The reference experiments form elongated, well-confined lobes. The fine deposit ($L/W \approx 1.7$; Figs. 4a and 5a) tapers gradually downslope, reaching a runout length of 146 cm and covering an area of 1.1 $\mathrm{m^2}$ with a volume of 71 L. The coarse deposit ($L/W \approx 2.2$; Figs. 4b and 5b) is isolated on the runout area, as all material was released from the channel, extending to a maximum runout of 245 cm, an area of 1.9 $\mathrm{m^2}$, and a volume of 83 L. In both size fractions, the centers of volume are located near the top-view midpoint of the deposit.

The Glass experiments produce elongated lobes with undulating surfaces, but their shape differs markedly between the fine and coarse debris flow. The fine deposit (Glass/f; Figs. 4a and 5a) forms a well-confined lobe ($L/W \approx 1.7$) with clear lateral margins and decreases gradually in height downslope. It's length of 157 cm, area of 1.3 $\mathrm{m^2}$, and volume of 75 L resemble the fine reference experiment. The center of volume lies near the plan-view midpoint. The coarse deposit (Glass/c; Figs. 4b and 5b) is distinctly more stretched ($L/W \approx 2.4$) reaching with 303 cm almost twice the length and covering with 2.9 $\mathrm{m^2}$ an area roughly double in size. The volume of 89 L is only by <20% larger. The deposit consists of two parts: a compact main body extending over the first 2 m, gradually decreasing in height, and a 1 m long, flat ($\leq$ 1 cm) frontal fringe composed of loosely dispersed particles. The center of volume is located approximately halfway along the main body.

The Qtz and Mag experiments yield almost identical deposit shapes and contour patterns within each size fraction. The fine deposits (Qtz/f and Mag/f; Figs. 4a and 5a) are compact, with runout lengths and widths being nearly equal ($L/W \approx 1.0$).

https://doi.org/10.5194/egusphere-2026-1235
Preprint. Discussion started: 19 March 2026

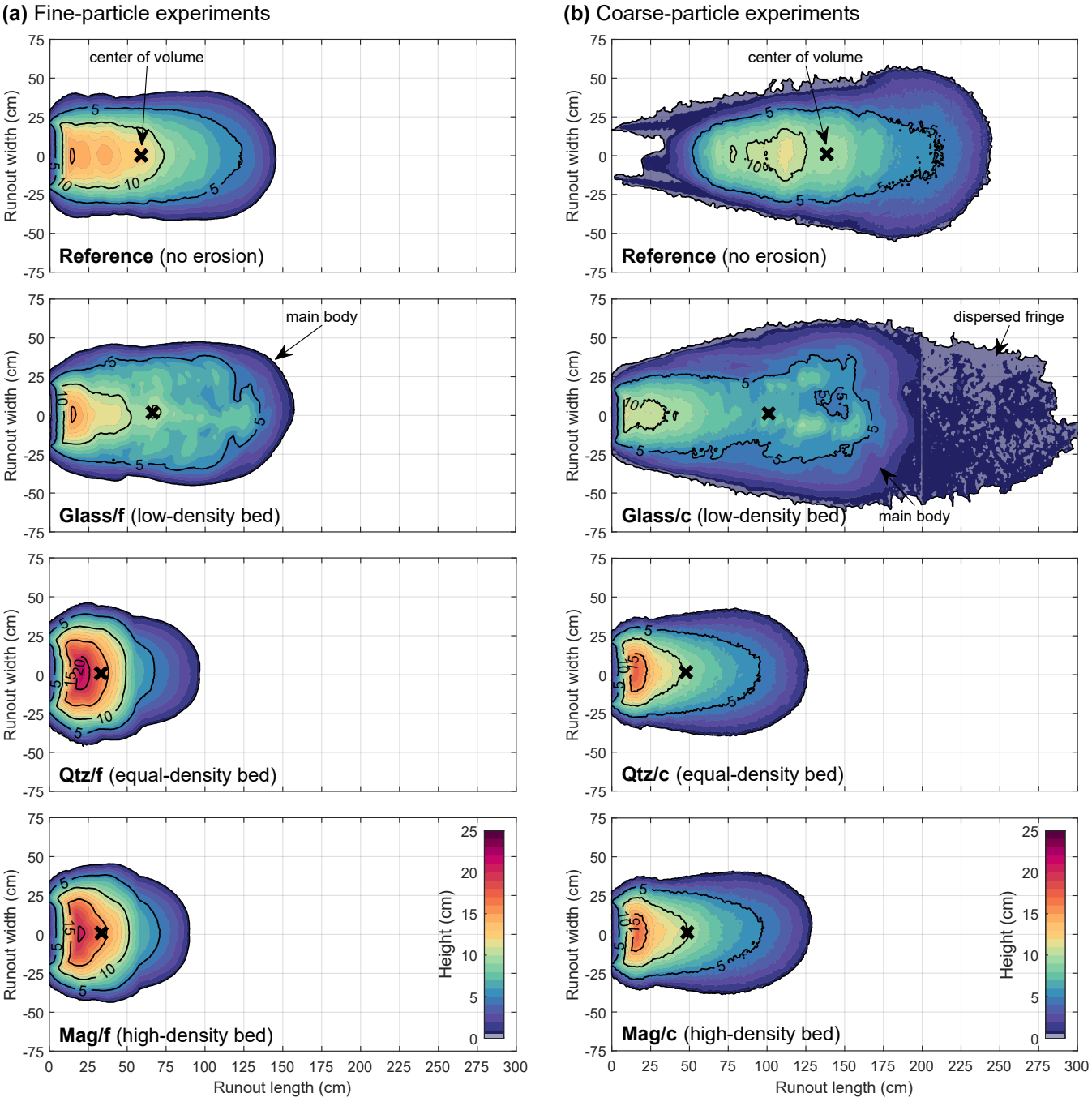

Figure 4. Deposit morphology of (a) fine- and (b) coarse-particle experiments. From top to bottom: contours of deposit height for the reference case without erosion, the glass bed, the quartz bed, and the magnetite bed. Representative runs are shown (see Sect. 2.4). Note that the flume was repositioned to the horizontal before deposit scanning; therefore, only material deposited beyond the flume outlet was analyzed, and the apparent thickness drop towards $(0|0)$ is a systematic artifact (see Supplement Fig. S5). /f: fine particles; /c: coarse particles.

https://doi.org/10.5194/egusphere-2026-1235
Preprint. Discussion started: 19 March 2026

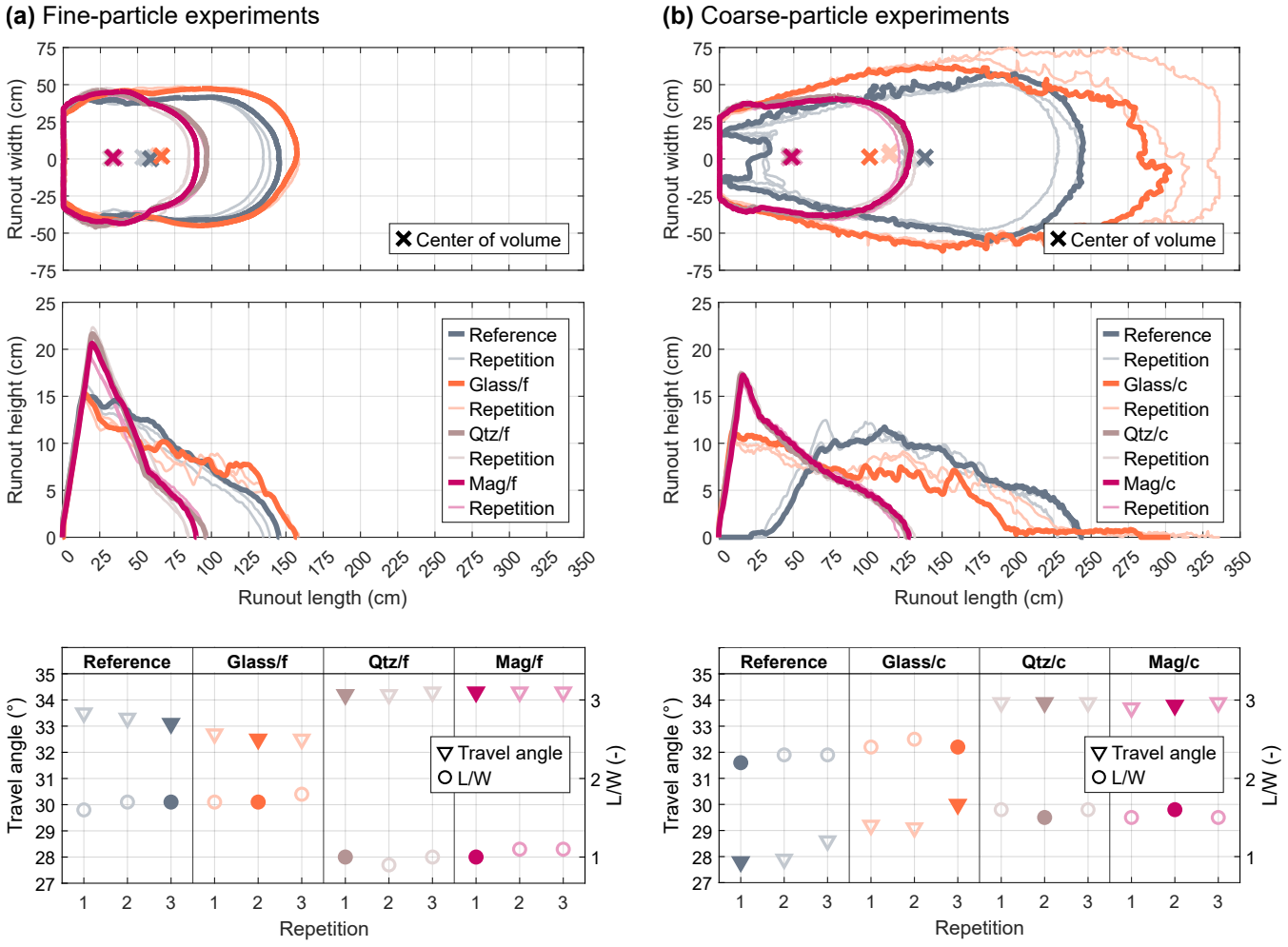

Figure 5. Deposit geometry and experimental reproducibility for (a) fine- and (b) coarse-particle experiments. From top to bottom: deposit outlines, downslope runout height along the central deposit line, as well as travel angle and L/W for all repetitions. Bold lines and filled symbols indicate the representative runs (see Sect. 2.4); thin lines or open symbols show their repetitions. /f: fine particles; /c: coarse particles; L/W: length-to-width ratio.

Along the centerline, runout height shows an initial steep decrease that transitions to a gentler gradient beyond a distinct break in slope (at ~55 cm length). Runout lengths are short with 90–97 cm, and cover a small area of 0.7 m^2 with volumes of ~52 L. The coarse deposits (Qtz/c and Mag/c; Figs. 4b and 5b) are more elongated ($L/W \approx 1.5$) and show two breaks in slope in their downslope height profiles (at ~25 and 75 cm length). Their runouts are both nearly 130 cm long, covering an area of 0.9 m^2 and a volume of ~50 L. In both size fractions, the centers of volume remain close to the channel outlet.

https://doi.org/10.5194/egusphere-2026-1235
Preprint. Discussion started: 19 March 2026

3.2.2 Internal deposit structure

Lateral cross sections through the Qtz–Glass and Qtz–Mag deposits reveal distinct internal sorting and spatial patterns in both fine (Supplement Fig. S8) and coarse experiments (Fig. 6). The mixed slide–bed deposits show a finer-grained core that coarsens toward the deposit surface (cross-checks of the Qtz–Qtz and reference deposits confirmed comparable sorting). The sorting is particularly evident in the coarse experiments, where the particle-size spectrum is wider. The material distribution, however, differs between the bed materials.

In the Glass experiments (Fig. 6a and Supplement Fig. S8a), a sharp boundary occurs between the two materials. Qtz–slide particles are concentrated in the interior of the main body, while Glass-bed particles form the lateral edges. With increasing runout distance, the lateral Glass edges widen and the central Qtz core narrows. In the intermediate sections, Glass particles appear laterally shouldered onto a thin Qtz layer and the central Qtz core becomes disrupted by distinct Glass ridges. Toward the distal end of the main body, the deposits consist almost entirely of Glass. In the fine deposit (Glass/f; Supplement Fig. S8a), Glass also appears centrally along the deposit base. In the coarse deposit (Glass/c; Fig. 6a), the frontal meter consists of a fringe mainly composed of loosely dispersed coarse Glass with only a few Qtz particles.

In the Mag experiments (Figs. 6b and Supplement Fig. S8b), material separation is less distinct due to the similar material colors. The deposits appear to be dominated by Qtz–slide particles, whereas Mag-bed particles occur rather as localized clusters. In the fine deposit (Mag/f; Supplement Fig. S8b), Mag particles are concentrated at the edges and within thin basal layers. In the coarse deposit (Mag/c; Fig. 6b), Mag particles form lateral lenses and individual cluster along the deposit base and become largely absent toward the deposit front.

4 Discussion

Following the inertia-based mobility concept of Pudasaini and Krautblatter (2021), our experiments span three energy regimes arising from density differences between an initial Qtz–slide and a low-density Glass bed (inertially weak scenario), an equal-density Qtz bed (inertially neutral scenario), and a high-density Mag bed (inertially strong scenario). Reference experiments conducted over a rigid bed provide a baseline for debris-flow behavior without erosion. Across these four scenarios, the data vary systematically, with close agreement between repeated runs (Supplement Figs. S1-S4, S6, S7), supporting the use of a single representative run per scenario and demonstrating the reproducibility of the trends discussed below.

4.1 Flow–bed inertia and its expression in debris-flow mobility and runout

Distinct material-dependent patterns are consistently expressed in both the spatiotemporal debris-flow evolution (Sect. 3.1) and the resulting deposit geometry (Sect. 3.2). Particularly clear contrasts emerge when comparing the inertially weak and inertially neutral scenarios. On the Glass beds, greater erosion depths and higher apparent mean erosion rates are accompanied

https://doi.org/10.5194/egusphere-2026-1235
Preprint. Discussion started: 19 March 2026

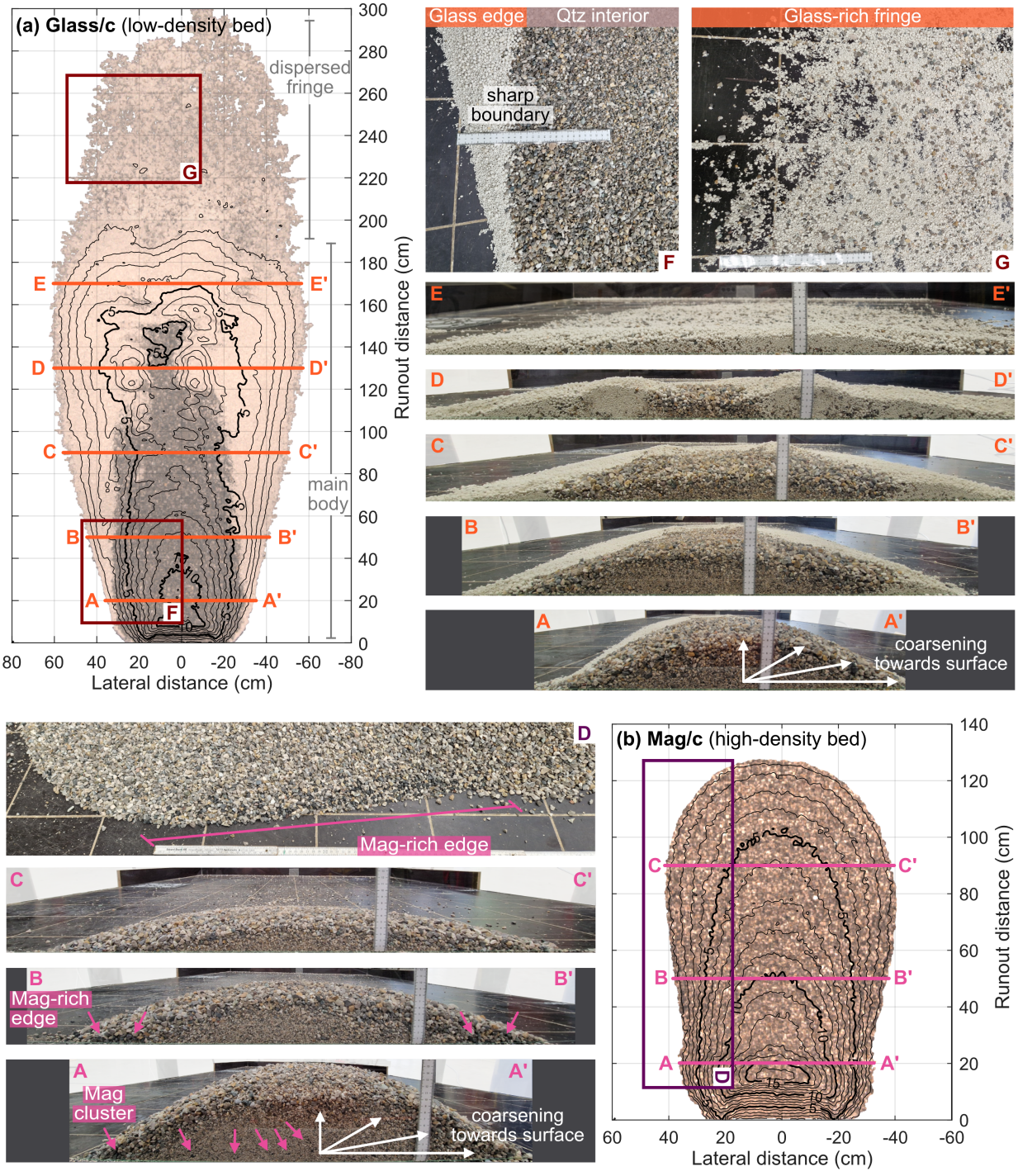

Figure 6. Internal structure and spatial distribution of a (a) Qtz–Glass and (b) Qtz–Mag deposit from coarse-particle experiments. Positions of lateral cross sections and surface views are indicated on the contoured surface scan. Contour lines are spaced at 1 cm intervals. Note that thicknesses in the cross sections may appear slightly reduced compared to the corresponding contour-plot position, as inserting the glass plate for vertical cutting could drag material downward at the front. Photographs are from Exp18 (Glass/c) and Exp19 (Mag/c).

https://doi.org/10.5194/egusphere-2026-1235
Preprint. Discussion started: 19 March 2026

by increasing flow-front velocities, whereas erosion on the Qtz beds is less pronounced and flow-front velocities remain nearly constant once erosion begins (Fig. 3). This contrast indicates greater entrainment and higher mobility for the low-density Glass bed, when compared to neutral conditions. Consistent with this behavior, the Qtz–Glass deposits are approximately 1.6 times longer than the Qtz–Qtz deposits and cover nearly twice the area when only considering the main deposit body in both size fractions (Fig. 4). In the case of Glass/c, including the dispersed frontal fringe increases total runout even to more than twice that of Qtz/c and expands the covered area by more than a factor of three. The internal Qtz–Glass-deposit structures further reflect the strong density contrast in the inertially weak scenarios, with the light Glass particles preferentially transported toward the fronts and lateral edges, while Qtz particles form dense central cores. For Glass/c, this phase separation is particularly evident as dispersed, Glass-dominated fringe ahead of the main deposit body (Fig. 6a). Strikingly, the inertially strong scenarios do not exhibit a systematic reduction in mobility relative to the inertially neutral scenarios. Instead, erosion, flow-front velocity and deposit characteristics are fairly congruent between the Mag and Qtz beds. The internal Qtz–Mag-deposit structures indicate only limited incorporation of the heavy Mag particles. The deposits are dominated by Qtz–slide particles, while Mag-bed particles occur only as sparse clusters or thin lateral lenses (Fig. 6b). Finally, consistent with the expectation by Pudasaini and Krautblatter (2021), our experiments show enhanced mobility and extended runout when the debris flows entrain material from the low-density beds in the inertially weak scenarios, relative to the inertially neutral scenarios. However, the entrainment of significantly denser bed material does not result in the anticipated mobility reduction in the inertially strong scenarios under the experimental conditions considered here. Instead, both equal- and high-density beds lead to comparable deceleration of the debris flow, suggesting similar and higher energy consumption and momentum loss during bed erosion and entrainment compared to the low-density material. Consequently, when considering only externally observable flow and deposit characteristics, and not intrinsic process dynamics, our results based on density contrasts alone do not provide sufficient support for the inertia-based mobility hypothesis proposed by Pudasaini and Krautblatter (2021).

The presence of an erodible bed noticeably alters debris-flow evolution. Flow fronts steepen immediately upon arrival at the erodible bed, as the basal roughness abruptly increases compared to the rigid plywood surface, decelerating the flow. The erosive scenarios therefore consistently exhibit reduced frontal acceleration and lower flow-front velocities compared to the reference scenarios without erosion, beyond local bed-surface lowering (Fig. 3). This behavior is consistent with previous flume studies showing that erosion increases flow resistance since part of the available energy is consumed by entrainment processes (e.g., Tian et al., 2014; Li et al., 2022). In our experiments, this additional energy dissipation during erosion leads to shorter runouts, except in the inertially weak scenarios where the lengths of the main deposit bodies are comparable to the reference scenarios (Fig. 4).

Distinct erosion and entrainment modes are evident from the temporal evolution of flow heights over the erodible beds (Fig. 3). Whereas the Glass beds are eroded rapidly in a stepwise manner, the Qtz and Mag beds exhibit more progressive grain-by-grain entrainment. These entrainment mechanisms were identified before by De Haas and Van Woerkom (2016) using colored erodible beds, where entrainment through localized en-masse failure was inferred from the deposition of largely intact color layers, in contrast to grain-by-grain entrainment associated with more homogeneous color mixing. Roelofs et al. (2023)

https://doi.org/10.5194/egusphere-2026-1235
Preprint. Discussion started: 19 March 2026

further showed that beds with a water content close to saturation tend to fail en-masse when overridden by debris flows. The similarity to the stepwise erosion observed in our inertially weak scenarios suggests that mechanically weak ground may exhibit comparable entrainment behavior, regardless of whether the weakness arises from high water content or low material density. Eventually, our apparent mean erosion rates span 0.3–1.2 $\mathrm{cm\,s^{-1}}$ (Table 2). These values overlap with the lower end of erosion rates reported from debris-flow flume experiments over partially saturated beds, including 0.3–1.8 $\mathrm{cm\,s^{-1}}$ reported by Zheng et al. (2021), but remain below the higher experimental ranges (e.g., 5–10 $\mathrm{cm\,s^{-1}}$ in Iverson et al. (2011) and Reid et al. (2011); 1.9–4.3 $\mathrm{cm\,s^{-1}}$ in Li et al. (2018)). They also compare well with field observations, where natural debris-flow events entrain at average rates of 1.1–14 $\mathrm{cm\,s^{-1}}$ over saturated beds and at 0.2–0.5 $\mathrm{cm\,s^{-1}}$ over dry beds (McCoy et al., 2012).

Fine and coarse experiments exhibit consistent patterns across the different inertial scenarios. Grain-size segregation is evident from all experiments, with coarse particles preferentially accumulated toward the deposit front and surface (Fig. 6), consistent to previous debris-flow experiments (e.g., De Haas and Van Woerkom, 2016; Baselt et al., 2022). This sorting may arise from a recirculation mechanism during flow. Whereas finer particles may segregate downward into the flow interior, coarse particles may progressively migrate upward by shear-induced segregation toward the faster-moving surface and be transported forward toward the flow front, where they can recirculate while being continuously advected toward the flow edges. As result, deposition fronts, surfaces, and lateral edges may become enriched in coarse particles (Johnson et al., 2012; Edwards et al., 2023). Within a given scenario, final erosion depths, apparent mean erosion rates, and flow-front velocities vary only marginally between both size fractions (Fig. 3). Erosion is slightly deeper and apparent mean erosion rates are slightly higher for the coarse experiments, which may reflect variations in bed packing. Coarser beds are typically more loosely packed, facilitating particle mobilization and erosion, while finer beds tend to be more densely packed and mechanically interlocked, which increases their resistance to particle entrainment under otherwise comparable flow conditions. Coarse debris flows pass the ultrasonic sensor stations slightly faster. This difference, however, is likely because releasing the same initial mass as Qtz–slide corresponds to a release volume that is approximately 10 L smaller for the coarser fraction due to its higher dry bulk density (Table 1). Despite these comparatively subtle differences in flow dynamics, the final deposit morphology markedly differs between both size fractions. Coarse experiments systematically produce longer, flatter, elongated lobes, whereas fine experiments yield shorter, thicker deposits (Figs. 4 and 5). In the inertially weak scenario, the coarse Qtz–Glass deposit additionally shows a more diffusive margin but remains more compact and laterally confined in the fine case. Yet, volumes on the runout area of fine and coarse deposits are similar, and even identical in the neutral and strong scenarios (Table 2). This decoupling between similar debris-flow dynamics during erosion and contrasting depositional geometries suggests that grain-size-dependent differences in basal friction further influence debris-flow mobility. In the erosive scenarios, fine and coarse debris flows exhibit similar surface and bulk flow behavior while traversing the erodible bed, the underlying resistance mechanisms, however, may differ. For example, the coarse Qtz–slide may dissipate more energy during erosion due to higher internal friction in the coarse beds (Table 1). Flume experiments have shown that coarse sediments exhibit greater resistance to erosion (Li et al., 2022). This could offset any tendency toward higher flow-front velocities of the coarse debris flows during this phase, and result in comparable velocities to the fine debris flows by the end of the erosive section. The reference scenarios support this interpretation. Under identical basal conditions along the entire flume channel, the coarse debris flows eventually accelerate more strongly on the rigid bed

https://doi.org/10.5194/egusphere-2026-1235
Preprint. Discussion started: 19 March 2026

and attain higher final flow-front velocities than the fine debris flows (Fig. 3). Once the debris flows then enter the common rigid runout area, coarse debris flows consistently travel farther (Fig. 4). These observations suggest that during deposition mobility and spreading are modulated by basal friction, which, on the same basal surface, is lower for coarse and higher for fine material. The fine material therefore dissipates kinetic energy more rapidly and comes to rest earlier.

4.2 Additional grain-scale controls on debris-flow mobility

Our experimental data only partly reflect the three energy regimes proposed by Pudasaini and Krautblatter (2021). While the inertially weak scenarios show the expected enhancement in mobility and runout relative to the inertially neutral scenarios, the inertially strong scenarios behave more similarly to the neutral case than anticipated (Figs. 3, 4, 5). Notably, despite an almost twofold difference in solid density between Mag and Qtz (Table 1), both scenarios produce very similar runout. This suggests that, solid density contrasts alone do not fully account for the observed mobility trends and depositional patterns among the different scenarios and that additional mechanisms acting at the grain scale may modulate the flow response and control momentum dissipation during erosion and entrainment, too. Below, we discuss the potential roles of (i) particle shape, (ii) friction, (iii) bed compaction, and (iv) particle segregation efficiency.

(i) Particle roundness is a key shape parameter that strongly affects the mechanical response of granular materials (e.g., Ali et al., 2023). Higher roundness reduces rolling resistance and facilitates particle rotation (Estrada et al., 2011), whereas angular particles exhibit stronger interlocking and higher shear strength, reducing the magnitude of rotation (Ali et al., 2023). In our experiments, the low-density Glass beds consist of artificial particles whose rounded, nearly spherical shapes differ markedly from the angular Qtz and Mag particles (Fig. 1). This geometrical material contrast suggests that, as the near-spherical Glass particles roll more easily, the Glass beds may be entrained more readily, promoting additional mobility. This interpretation is supported by the higher apparent mean erosion rates and higher final flow-front velocities in the Glass experiments (Fig. 3). These observations agree with findings from previous erosive debris-flow experiments, where higher particle roundness in erodible beds was found to reduce debris-flow resistance and enhance entrainment rates (Li et al., 2022). The influence of particle shape appears particularly evident in the far runout of Glass/c, where a dispersed frontal fringe composed almost entirely of coarse spherical Glass particles formed ahead of the main deposit body (Figs. 4b and 6a). In contrast, Glass/f does not form such a fringe but only a well-confined lobe (Figs. 4a and Supplement Fig. S8a). The more pronounced rolling behavior in Glass/c therefore implies that the coarse spherical particles may dissipate less energy to frictional and collisional interactions than the fine spherical particles on the same runout surface.

(ii) Once the slope exceeds a critical angle of roughly half the material's angle of repose, entrainment begins to affect the flow and may increase runout by up to 40% on slopes close to the repose angle (Mangeney et al., 2010). In our experiments, the flume inclination of 37° far exceeds the internal friction angles of Glass of ~30° (Table 1), which required additional stabilization of the bed to maintain the imposed steep inclination (Sect. 2.2). The Glass bed was therefore effectively inclined beyond its stability limit during the experiments, offering relatively little shear resistance. This low stability allowed particles to be eroded and entrained with comparatively little mechanical forcing, likely contributing to the enhanced mobility and long

https://doi.org/10.5194/egusphere-2026-1235
Preprint. Discussion started: 19 March 2026

runout observed in the inertially weak scenarios. In contrast, the internal friction angles of Qtz and Mag lie close to the 37° flume inclination (Table 1), meaning these beds were operated near their natural stability limits. Under these conditions, the Qtz and Mag beds were comparatively resistant to disturbance, making entrainment more difficult and energetically demanding. The similarity in their frictional behavior and comparable resistance to shearing and deformation may help to explain why both materials, despite contrasting densities, display nearly identical flow evolution, erosion depths and deposits (Figs. 3, 4, 5). Interface tests further support this interpretation, showing that a Qtz layer begins to slide on a Mag bed at inclinations of 38° and 39° for the fine and coarse fraction, respectively. These values closely match the internal friction angles of Qtz of 37° and 39°, respectively (Table 1). The influence of internal friction on bed stability and entrainment may also be reflected in the observed travel angles, commonly used as an indicator of apparent friction (e.g., Parez and Aharonov, 2015; Taylor-Noonan et al., 2022). Our derived travel angles are systematically lower in the inertially weak scenarios compared to the neutral and strong cases (Fig. 5). This difference is particularly pronounced in the coarse experiments, where Glass/c yields travel angles of 29–30°, whereas Qtz/c and Mag/c consistently exhibit values around 34°. These lower travel angles may indicate overall reduced apparent friction and enhanced mobility in the inertially weak scenarios. Comparable travel angles of 28–29° were reported by Taylor-Noonan et al. (2022) for dry granular flows composed of near-spherical ~4 mm beads, supporting the plausibility of the observed values.

(iii) Compaction alters bed porosity and affects the shear strength and resistance of the bed. Higher levels of bed compaction have been observed to reduce the erosion depth and erosion rate (Bahmanpouri et al., 2021). Whereas the Qtz and Mag beds were prepared by simple infilling, the low-density Glass beds required slight surficial compaction to maintain the imposed 37° flume inclination. Among the coarse Glass repetitions (Exp16–Exp18), variations in this compaction step appear to have influenced runout length and deposit symmetry (Supplement Fig. S7b). Solely Exp17 was prepared by a different person and appeared to have received less and more uneven compaction during preparation, producing the farthest and most oblique runout. We note, however, that this inference is purely observational, as compaction was not directly measured. These compaction differences may have influenced the initial entrainment of surficial Glass-bed particles and subsequently the extent of the dispersed fringe. However, the differences were not large enough to affect the overall erosion depth.

(iv) Density differences between particles can drive segregation in granular flows even when particle sizes are equal, as buoyancy and drag act to different extents on particles of contrasting density (e.g., Tripathi and Khakhar, 2013; Gray and Ancey, 2015). In our experiments, the different patterns in material separation among Qtz–Glass and Qtz–Mag deposits (Fig. 6) can be attributed to differences in both particle density and shape, which together control segregation efficiency during erosion, entrainment, and deposition. In the Glass experiments, low-density Glass particles initially form the erodible bed, which is overridden by the denser Qtz–slide. This represents a mechanically unstable density configuration, in which lighter particles are forced beneath heavier ones. This instability promotes strong density-driven segregation, with denser Qtz particles migrating downward to form a basal, momentum-dominated core, while entrained Glass particles migrate upward through kinetic sieving and buoyancy. The nearly spherical shape of the Glass particles further facilitates this upward migration by reducing interlocking and rolling resistance. Consequently, Glass particles are preferentially transported toward the flow surface,

https://doi.org/10.5194/egusphere-2026-1235
Preprint. Discussion started: 19 March 2026

margins, and front, forming Qtz–Glass deposits with sharp material boundaries defined by Glass-dominated fronts and lateral edges (Fig. 6a). In contrast, the Mag experiments represent a mechanically stable density configuration, with the denser Mag particles remaining preferentially in the lower part of the flow once entrained. This promotes vertical density stratification but limits upward particle migration. In addition, the angularity of Qtz and Mag particles enhances interlocking and frictional coupling during motion, further restricting relative particle mobility. As a result, segregation in the Qtz–Mag deposits is expressed mainly as weak clustering or thin basal lenses, rather than as pronounced segregated domains (Fig. 6b).

4.3 Limitations and future steps

Our newly developed debris-flow flume produced highly reproducible flow and deposition signals and robust patterns across repeated runs (Supplement Fig. S1). This provides a solid basis for testing theoretical debris-flow models as well as for future experimental analyses of erosion and entrainment processes at the slide–bed interface. Nevertheless, certain experimental boundary conditions need to be considered when interpreting the results and point toward directions for future refinement and research.

The selection of the low-density material for the inertially weak scenario was constrained by the need for efficient post-experiment separation from Qtz and reusability, leading to the use of artificial expanded Glass. However, because the Glass differs from the natural materials Qtz and Mag by its round particle shape and lower internal frictional resistance, it likely has introduced additional mobility-enhancing effects beyond density-related effects (see Sect. 4.2). Future experiments could explore natural alternatives with an intermediate low density, such as limestone (~1700 $\mathrm{kg\,m^{-3}}$), with comparable particle angularity and frictional behavior, though, post-experiment separation remains challenging.

Comparing the inertially neutral and strong scenarios, it is possible that the in-channel backlog and deposition obscures subtle differences that might otherwise become apparent under full release onto the runout area. Since the flow fronts entered the runout area with similar velocities (Fig. 3) and were dominantly composed of Qtz particles (Fig. 6b and Supplement Fig. S8b), both scenarios initially experience comparable frictional resistance and rapid deceleration on the 10° inclined runout surface. As a result, the frontal material deposited quickly, limiting the visibility of possible differences at later flow stages. As a result, the deposits of the two scenarios may appear similar on the runout area, while any differences might instead be expressed in the in-channel deposit, which was not analyzed with 3D surface scanning. Yet, the congruent temporal evolution of flow height on the erodible bed and the similar timing and magnitude of excavation (Fig. 3) suggest that the overall intensity of entrainment in both scenarios is broadly comparable. Likewise, the nearly identical final erosion depths indicate that any differences between the Qtz and Mag experiments, if present at all, are likely to be small and may be difficult to distinguish from the scattering that such large experimental setups naturally hold.

Our erosion rates represent apparent mean estimates derived from the final erosion depth at a single location (Fig. 3). These mean rates therefore do not resolve temporal changes in erosion intensity. Although the Qtz and Mag hydrographs appear nearly congruent, the ultrasonic measurements do not allow to distinguish temporal changes in the elevation of the slide–bed

https://doi.org/10.5194/egusphere-2026-1235
Preprint. Discussion started: 19 March 2026

interface from changes in the thickness of the overlying Qtz–slide, as both contribute to flow height. Consequently, the inertially neutral and strong scenarios could exhibit subtly different entrainment dynamics at the flow base while still producing similar flow-height curves, final erosion depths, and deposit morphologies. For example, one scenario might undergo shorter but more intense erosion beneath a thicker slide, whereas the other erodes more gradually beneath a thinner slide. Yet, both could yield comparable flow-height signals. Such potential temporal small-scale nuances, however, remain inaccessible within this study. To resolve such temporal processes at depth and at the grain scale, direct observations of particle motion at the erodible bed will be required. Previous studies have applied particle tracking velocimetry (PTV) to resolve the vertical velocity structure in coarse-grained flows and examine particle interactions. Over erodible beds, Lanzoni et al. (2017) showed that vertical velocity profiles exhibit a gradual transition between coexisting rheological regimes, where frictional stresses prevail near the bed and collisional stresses dominate the upper flow region. Over rigid beds, Taylor-Noonan et al. (2022) identified distinct vertical flow regimes that control energy dissipation and mobility, with strong shear and energy expenditure concentrated at the flow base beneath a fast-moving core characterized by low shear strain rates that largely controls runout. Building on these approaches, PTV offers a means to analyze individual particle trajectories and derive vertical velocity profiles across the slide–bed interface. Such vertical velocity profiles would provide particle-scale quantities needed to further relate the erosion and entrainment processes in our experiments to the mechanistic descriptions of debris-flow mobility across the three energy regimes proposed by Pudasaini and Krautblatter (2021). Given the close similarity between our Qtz and Mag datasets, distinguishing these processes from natural experimental scattering will be challenging, but PTV seems promising to resolve subtle grain-scale dynamics at depth that might otherwise be obscured in our surface-based measurements.

Finally, the present study focused on dry granular single-phase debris-flow experiments to isolate the influence of inertial contrasts arising solely from different solid-density material combinations. However, water is a key component of natural debris flows, and its presence modifies erosion dynamics, flow momentum, and mobility, as demonstrated in previous experimental studies (e.g., De Haas and Van Woerkom, 2016; Iverson et al., 2011; Roelofs et al., 2023). A next step is therefore to investigate two-phase debris flows by recreating weak, neutral, and strong inertial contrasts through controlled variations in bed and slide water content. Moreover, previous studies indicate that erosion rate estimates often are higher if water is present (Iverson et al., 2011; Reid et al., 2011; McCoy et al., 2012), which may amplify mechanical contrasts and make subtle process differences more detectable.

5 Conclusions

This study experimentally tested the theoretical landslide mobility model, proposed by Pudasaini and Krautblatter (2021), which predicts that inertia governs the erosion-induced momentum transfer between slide and bed and thereby debris-flow mobility and runout. By releasing a slide of constant solid density over an erodible bed of lower, equal, or higher solid density, we approximated inertially weak, neutral, or strong conditions to examine the effect of inertia on erosion, debris-flow mobility, and runout based on measurements of flow and deposit surface. Our analyses lead us to the following main findings:

https://doi.org/10.5194/egusphere-2026-1235
Preprint. Discussion started: 19 March 2026

(i) Inertially weak scenarios with low-density beds show enhanced erosion, higher flow-front velocities, and longer runout than inertially neutral scenarios with equal-density beds, in agreement with the model prediction of increased debris-flow mobility. In contrast, inertially strong scenarios with high-density beds do not exhibit the predicted mobility reduction. Instead, erosion, flow-front velocities, and deposit geometries are similar to those of the inertially neutral scenarios, despite the substantially denser bed.

(ii) Solid density contrast alone is therefore insufficient to explain the observed mobility and runout patterns. Particle shape and internal friction exert a strong influence on debris-flow behavior. In the inertially weak scenarios, the spherical shape and low internal friction angle of the low-density material reduce shear and rolling resistance, enhancing entrainment efficiency and mobility beyond what is expected from density contrast alone. In contrast, in the inertially neutral and strong scenarios, the angular shape and similar high internal friction angles of the equal-density and high-density material promote stronger particle interlocking, resulting apparently in comparable debris-flow mobility.

(iii) Repeating the experiments for a sand and sand–gravel mixture shows that particle-size distribution does not affect the relative patterns among the inertial scenarios but mainly controls depositional spreading through grain-size-dependent basal friction.

Consequently, a surface-based evaluation of flow and deposit characteristics alone is insufficient for a density-controlled interpretation of erosion-induced mobility changes. Resolving intrinsic process dynamics, such as vertical velocity profiles or tracking individual bed particles during entrainment across the slide–bed interface, will be necessary to identify subtle differences in entrainment mechanisms and momentum dissipation that are not detectable from bulk observations alone.

Data availability. The experimental datasets of this study will be made freely available in an accompanying data publication via Open Data UniBw M upon full publication

Author contributions. IB, SPP, and MK conceived the project. KW and IB developed the conceptual design of the experimental flume. SM carried out the technical implementation of the flume. KW conducted the experiments and analyzed the data. KW prepared the initial draft, figures, and tables, and adjusted the manuscript based on the comments and edits of all co-authors.

Competing interests. The authors declare that they have no conflict of interest.

Acknowledgements. This research was funded by the Deutsche Forschungsgemeinschaft (DFG, German Research Foundation) – Project number: 522201978. We thank the staff of the Hydraulic Laboratory for their technical support in constructing the experimental set-up and for their assistance during the experiments.

https://doi.org/10.5194/egusphere-2026-1235
Preprint. Discussion started: 19 March 2026

References

Ali, U., Kikumoto, M., Ciantia, M., Cui, Y., and Previtali, M.: Systematic effect of particle roundness/angularity on macro-and microscopic behavior of granular materials, Granular Matter, 25, 51, https://doi.org/10.1007/s10035-023-01341-y, 2023.

Bahmanpouri, F., Daliri, M., Khoshkonesh, A., Namin, M. M., and Buccino, M.: Bed compaction effect on dam break flow over erodible bed; experimental and numerical modeling, Journal of Hydrology, 594, 125 645, https://doi.org/10.1016/j.jhydrol.2020.125645, 2021.

Baselt, I., de Oliveira, G. Q., Fischer, J.-T., and Pudasaini, S. P.: Deposition morphology in large-scale laboratory stony debris flows, Geomorphology, 396, 107 992, https://doi.org/10.1016/j.geomorph.2021.107992, 2022.

Berger, C., McArdell, B., and Schlunegger, F.: Direct measurement of channel erosion by debris flows, Illgraben, Switzerland, Journal of Geophysical Research: Earth Surface, 116, https://doi.org/10.1029/2010JF001722, 2011.

De Haas, T. and Van Woerkom, T.: Bed scour by debris flows: Experimental investigation of effects of debris-flow composition, Earth Surface Processes and Landforms, 41, 1951–1966, https://doi.org/10.1002/esp.3963, 2016.

De Haas, T., Braat, L., Leuven, J. R., Lokhorst, I. R., and Kleinhans, M. G.: Effects of debris flow composition on runout, depositional mechanisms, and deposit morphology in laboratory experiments, Journal of Geophysical Research: Earth Surface, 120, 1949–1972, https://doi.org/10.1002/2015JF003525, 2015.

De Haas, T., Nijland, W., De Jong, S., and McArdell, B.: How memory effects, check dams, and channel geometry control erosion and deposition by debris flows, Scientific reports, 10, 14 024, https://doi.org//10.1038/s41598-020-71016-8, 2020.

Edwards, A., Rocha, F., Kokelaar, B., Johnson, C., and Gray, J.: Particle-size segregation in self-channelized granular flows, Journal of Fluid Mechanics, 955, A38, https://doi.org/10.1017/jfm.2022.1089, 2023.

Egashira, S., Honda, N., and Itoh, T.: Experimental study on the entrainment of bed material into debris flow, Physics and Chemistry of the Earth, Part C: Solar, Terrestrial & Planetary Science, 26, 645–650, https://doi.org/10.1016/S1464-1917(01)00062-9, 2001.

Estrada, N., Azéma, E., Radjai, F., and Taboada, A.: Identification of rolling resistance as a shape parameter in sheared granular media, Physical Review E—Statistical, Nonlinear, and Soft Matter Physics, 84, 011 306, https://doi.org/10.1103/PhysRevE.84.011306, 2011.

Frank, F., McArdell, B. W., Huggel, C., and Vieli, A.: The importance of entrainment and bulking on debris flow runout modeling: examples from the Swiss Alps, Natural Hazards and Earth System Sciences, 15, 2569–2583, https://doi.org/10.5194/nhess-15-2569-2015, 2015.

Gray, J. and Ancey, C.: Particle-size and-density segregation in granular free-surface flows, Journal of Fluid Mechanics, 779, 622–668, https://doi.org/10.1017/jfm.2015.438, 2015.

Hungr, O., McDougall, S., and Bovis, M.: Entrainment of material by debris flows, in: Debris-flow hazards and related phenomena, pp. 135–158, Springer, 2005.

Iverson, R. M.: Elementary theory of bed-sediment entrainment by debris flows and avalanches, Journal of Geophysical Research: Earth Surface, 117, https://doi.org/10.1029/2011JF002189, 2012.

Iverson, R. M., Reid, M. E., Logan, M., LaHusen, R. G., Godt, J. W., and Griswold, J. P.: Positive feedback and momentum growth during debris-flow entrainment of wet bed sediment, Nature Geoscience, 4, 116–121, https://doi.org/10.1038/NGEO1040, 2011.

Johnson, C., Kokelaar, B., Iverson, R. M., Logan, M., LaHusen, R., and Gray, J.: Grain-size segregation and levee formation in geophysical mass flows, Journal of Geophysical Research: Earth Surface, 117, https://doi.org/10.1029/2011JF002185, 2012.

Lanzoni, S., Gregoretti, C., and Stancanelli, L. M.: Coarse-grained debris flow dynamics on erodible beds, Journal of Geophysical Research: Earth Surface, 122, 592–614, https://doi.org/10.1002/2016JF004046, 2017.

https://doi.org/10.5194/egusphere-2026-1235
Preprint. Discussion started: 19 March 2026

Li, P., Hu, K., and Wang, X.: Debris flow entrainment rates in non-uniform channels with convex and concave slopes, Journal of Hydraulic Research, 56, 156–167, https://doi.org/10.1080/00221686.2017.1313321, 2018.

Li, P., Wang, J.-d., Hu, K.-h., Qiu, H.-j., and Xie, J.-l.: Experimental investigation on debris flow resistance and entrainment characteristics: effects of the erodible bed with discontinuous grading, Journal of Mountain Science, 19, 2397–2419, https://doi.org/10.1007/s11629-022-7365-y, 2022.

Liu, H., Zhao, X., Frattini, P., Crosta, G. B., De Blasio, F. V., Wan, Y., and Zhu, X.: Mobility and erosion of granular flows travelling on an erodible substrate: Insights from the small-scale flume experiments, Engineering Geology, 326, 107 316, https://doi.org/10.1016/j.enggeo.2023.107316, 2023.

Lu, P.-y., Yang, X.-g., Xu, F.-g., Hou, T.-x., and Zhou, J.-w.: An analysis of the entrainment effect of dry debris avalanches on loose bed materials, SpringerPlus, 5, 1621, https://doi.org/10.1186/s40064-016-3272-4, 2016.

Mangeney, A., Tsimring, L., Volfson, D., Aranson, I. S., and Bouchut, F.: Avalanche mobility induced by the presence of an erodible bed and associated entrainment, Geophysical Research Letters, 34, https://doi.org/10.1029/2007GL031348, 2007.

Mangeney, A., Roche, O., Hungr, O., Mangold, N., Faccanoni, G., and Lucas, A.: Erosion and mobility in granular collapse over sloping beds, Journal of Geophysical Research: Earth Surface, 115, https://doi.org/10.1029/2009JF001462, 2010.

McCoy, S., Kean, J. W., Coe, J. A., Tucker, G., Staley, D. M., and Wasklewicz, T.: Sediment entrainment by debris flows: In situ measurements from the headwaters of a steep catchment, Journal of Geophysical Research: Earth Surface, 117, https://doi.org/10.1029/2011JF002278, 2012.

McDougall, S. and Hungr, O.: Dynamic modelling of entrainment in rapid landslides, Canadian Geotechnical Journal, 42, 1437–1448, https://doi.org/10.1139/t05-064, 2005.

Medina, V., Hürlimann, M., and Bateman, A.: Application of FLATModel, a 2D finite volume code, to debris flows in the northeastern part of the Iberian Peninsula, Landslides, 5, 127–142, https://doi.org/10.1007/s10346-007-0102-3, 2008.

Pandey, N. K. and Satyam, N.: Entrainment-driven morphological changes in debris flow deposits by varying water content at laboratory scale, Bulletin of Engineering Geology and the Environment, 84, 1–24, https://doi.org/10.1007/s10064-025-04241-y, 2025.

Papa, M., Egashira, S., and Itoh, T.: Critical conditions of bed sediment entrainment due to debris flow, Natural Hazards and Earth System Sciences, 4, 469–474, https://doi.org/10.5194/nhess-4-469-2004, 2004.

Parez, S. and Aharonov, E.: Long runout landslides: a solution from granular mechanics, Frontiers in Physics, 3, 80, https://doi.org/10.3389/fphy.2015.00080, 2015.

Pudasaini, S. P. and Fischer, J.-T.: A mechanical erosion model for two-phase mass flows, International Journal of Multiphase Flow, 132, 103 416, https://doi.org/10.1016/j.ijmultiphaseflow.2020.103416, 2020.

Pudasaini, S. P. and Krautblatter, M.: The mechanics of landslide mobility with erosion, Nature communications, 12, 6793, https://doi.org/10.1038/s41467-021-26959-5, 2021.

Reid, M. E., Iverson, R. M., Logan, M., Lahusen, R. G., Godt, J. W., and Griswold, J. P.: Entrainment of bed sediment by debris flows: results from large-scale experiments, Italian journal of engineering geology and environment, pp. 367–374, https://doi.org/10.4408/IJEGE.2011-03.B-042, 2011.

Rickenmann, D.: Empirical relationships for debris flows, Natural hazards, 19, 47–77, 1999.

Roelofs, L., Colucci, P., and de Haas, T.: How debris-flow composition affects bed erosion quantity and mechanisms: An experimental assessment, Earth Surface Processes and Landforms, 47, 2151–2169, https://doi.org/10.1002/esp.5369, 2022.

https://doi.org/10.5194/egusphere-2026-1235
Preprint. Discussion started: 19 March 2026

Roelofs, L., Nota, E. W., Flipsen, T. C., Colucci, P., and de Haas, T.: How bed composition affects erosion by debris flows—An experimental assessment, Geophysical Research Letters, 50, e2023GL103 294, https://doi.org/10.1029/2023GL103294, 2023.

Santi, P. M., DeWolfe, V. G., Higgins, J. D., Cannon, S. H., and Gartner, J. E.: Sources of debris flow material in burned areas, Geomorphology, 96, 310–321, https://doi.org/10.1016/j.geomorph.2007.02.022, 2008.

Taylor-Noonan, A. M., Bowman, E. T., McArdell, B. W., Kaitna, R., McElwaine, J. N., and Take, W. A.: Influence of pore fluid on grain-scale interactions and mobility of granular flows of differing volume, Journal of Geophysical Research: Earth Surface, 127, e2022JF006 622, https://doi.org/10.1029/2022JF006622, 2022.

Tian, M., Hu, K.-h., Ma, C., and Lei, F.-h.: Effect of bed sediment entrainment on debris-flow resistance, Journal of Hydraulic Engineering, 140, 115–120, https://doi.org/10.1061/(ASCE)HY.1943-7900.0000805, 2014.

Tripathi, A. and Khakhar, D.: Density difference-driven segregation in a dense granular flow, Journal of Fluid Mechanics, 717, 643–669, https://doi.org/10.1017/jfm.2012.603, 2013.

Zheng, H., Shi, Z., Yu, S., Fan, X., Hanley, K. J., and Feng, S.: Erosion mechanisms of debris flow on the sediment bed, Water Resources Research, 57, e2021WR030 707, https://doi.org/10.1029/2021WR030707, 2021.